On resolution sensitivity in the Community Atmosphere Model

Adam R. Herrington*& Kevin A. Reed
School of Marine and Atmospheric Sciences, Stony Brook University, Stony Brook, NY 11794
*Correspondence to: adam.herrington@stonybrook.edu

This paper describes...

Key Words: Climate models, physical parameterizations, resolution sensitivity

Received . . .

1. Introduction

An increasing number of Atmospheric General Circulation Models (AGCMs) are being developed to maximize efficiency on massively parallel systems, permitting regionally-refined high-resolution, or even globally high-resolution weather ($\Delta x \leq 5$ km) and climate ($\Delta x \leq 50$ km) simulations (Satoh *et al.* 2008; Skamarock *et al.* 2012; Zängl *et al.* 2014; Harris *et al.* 2016; Ullrich *et al.* 2017; Lauritzen *et al.* 2018). These models are built using unstructured meshes that allows for substantial grid flexibility, but lack physical parameterizations (*physics*) which behave consistently as the truncation scale of the model changes with different grid resolutions, referred to as scale-aware physics. The most common approach towards developing scale-aware physics is through the lens of limited area, large-eddy simulations (e.g., Plant and Craig 2008; Arakawa and Wu 2013; Song and Zhang 2018). By subsequently filtering large-eddy solutions to lower-resolution grids, a relationship between first- and higher-order moments may be understood and ultimately parameterized as a function of grid resolution. While this approach is necessary for developing scale-aware physics, it is not sufficient. The equations of motions have inherent scale dependencies, and the properties of dynamical modes are a function of native grid resolution (Orlanski 1981; Weisman *et al.* 1997; Pauluis and Garner 2006; Jeevanjee and Romps 2016). Scale-aware physics should also recognize these native grid dependencies.

The sensitivity of the Community Atmosphere Model (CAM; Neale *et al.* 2012), and its predecessor, the Community Climate Model (CCM) to resolution (*resolution* refers to *horizontal resolution* hereafter) is well documented through convergence studies (Kiehl and Williamson 1991; Williamson *et al.* 1995; Williamson 2008; Rauscher *et al.* 2013; Zarzycki *et al.* 2014; Herrington and Reed 2017). CAM/CCM is a fully supported, well-funded climate model, but despite thirty years of continual model development, there are robust sensitivities to resolution that have persisted in all versions of the model. This study argues that a unifying cause, the inherent scale sensitivities of the underlying dynamical equations, can explain the robust responses to resolution that occur in CAM/CCM.

In CAM/CCM, the atmosphere progressively dries with increasing resolution, seen through a reduction in simulated total precipitable water (Kiehl and Williamson 1991; Williamson *et al.* 1995; Williamson 2008; Rauscher *et al.* 2013; Zarzycki *et al.* 2014; Herrington and Reed 2017), which typically, but not always (see Williamson *et al.* 1995; Zarzycki *et al.* 2014), coincides with a reduction in cloud cover. Kiehl and Williamson (1991) and Williamson *et al.* (1995) suggested that the drying of the atmosphere is due to greater magnitude resolved vertical velocities with increasing resolution, with greater subsiding motion increasing the export of dry air from the upper troposphere. This mechanism is consistent with an analysis of moisture budgets in CAM, version 4 (CAM4; Neale *et al.* 2010) across multiple resolutions (Herrington and Reed 2017).

It is well known that the magnitude of vertical velocities increase with resolution in atmospheric models. While the cause of this sensitivity has been established for large-eddy simulations (see Jeevanjee 2017, and references therein), only recently has the vertical velocity field in AGCMs and their sensitivity to resolution received attention (Donner *et al.* 2016; O'Brien *et al.* 2016), albeit with seemingly conflicting explanations (Rauscher *et al.* 2016; Herrington and Reed 2018). To generalize the relationship between vertical velocity and resolution, let α refer to the ratio of W_0, the vertical velocity scale of some reference grid spacing Δx_0, to W, the vertical velocity scale for any Δx. A power law for α^{-1} in Δx is then,

$$\alpha^{-1} = \frac{W}{W_0} = \left(\frac{\Delta x}{\Delta x_0}\right)^n, \qquad (1)$$

where n is the power law exponent.

Rauscher *et al.* (2016) derive an estimate $n = h - 1$ in equation 1 by combining a scale analysis of the continuity equation with a power law representation Δx^{2h} of the second-order structure function of the horizontal wind. Strictly speaking, Δx here refers to the distance between two points for which the velocity increment is computed in the structure function, but with this distance set to the model grid-spacing. Regional models analyzed in Rauscher *et al.* (2016) provide evidence for $h < 1$, implying $n < 0$ and consistent with the increase in W with resolution in models.

Observations show that $h = \frac{1}{3}$ for horizontal scales on the order of 100 km and less (hereafter referred to as the *mesoscale*; Lindborg 1999; Cho and Lindborg 2001). This value for h is also supported by the slope of the kinetic energy spectrum $-\beta$, which can be related to the second-order structure function through the Weiner–Khinchine theorem, $\beta = (2h + 1)$, valid in the range $1 < \beta < 3$ (satisfies stationarity; Davis *et al.* 1996). For $h = \frac{1}{3}, \beta = \frac{5}{3}$, which is true for the kinetic energy spectrum in observations

(Nastrom and Gage 1985; Cho *et al.* 1999) and models at the mesoscale (e.g., Takahashi *et al.* 2006; Skamarock *et al.* 2014). Rauscher *et al.* (2016) propose that the overwhelming support for $h = \frac{1}{3}$ at the mesoscale provides an emergent constraint for $n = -\frac{2}{3}$ in equation 1.

In large-eddy simulations, the sensitivity of vertical velocities to resolution is adequately explained by a scale analysis of the dynamical equations (Weisman *et al.* 1997; Pauluis and Garner 2006; Jeevanjee and Romps 2016). For hydrostatic scales relevant to AGCMs, a scale analysis of the Poisson equation gives $W \propto D^{-1}$, where D is the horizontal scale of buoyancy perturbations driving vertical motion (Herrington and Reed 2018). In CAM aqua-planet simulations, the largest source of buoyancy is from stratifrom cloud formation, which are grid-limited with horizontal scales set by the effective resolution of the model (i.e., some multiple of Δx; Skamarock 2011), indicating $n = -1$ in equation 1 (Herrington and Reed 2018). Herrington and Reed (2017) has shown that the $n = -1$ scaling does not explain the behavior of CAM4 in a convergence experiment, but follow-up studies (Herrington and Reed 2018; Herrington *et al.* 2019) indicate that the inadequacy of the $n = -1$ scaling is not definitive, due to large time-truncation errors associated with fixing the physics time-step (Δt_{phys}) across resolutions in that study.

Another robust response of the CAM/CCM lineage to resolution is an increase in stratiform precipitation rates at the expense of parameterized convective precipitation rates. Stratiform precipitation is sometimes referred to as grid-scale precipitation because unlike parameterized convection, it condenses moisture locally without any transport by unresolved eddies. The resolution dependent partitioning between the two different precipitation routines is shown in Figure 1, which is a bar-graph of the climatological, global mean stratiform and convective precipitation rates in prior CAM/CCM convergence studies. The tendency for precipitation rates to shift from the convection scheme to the stratiform scheme with resolution has been documented in other models (Pope and Stratton 2002; Rauscher *et al.* 2016; Terai *et al.* 2018), but none have provided a convincing explanation for this sensitivity. The studies of Kiehl and Williamson (1991), Williamson *et al.* (1995) and Williamson (2013) indicate that the practice of reducing Δt_{phys} with resolution should by itself reduce the convective precipitation rates, however Figure 1 (top row) indicates that convergence studies with fixed Δt_{phys} still show a reduction in convective precipitation rates with resolution.

In this study, a convergence experiment using CAM, version 6 (CAM6; `https://ncar.github.io/CAM/doc/build/html/users_guide/index.html`) is carried out and analyzed in detail. It is shown that the resolution sensitivity of vertical velocities are well described with $n = -1$ in equation (1), provided Δt_{phys} is defined in a way that avoids large truncation errors across resolutions. The increase in stratiform precipitation rates with resolution are attributed to an increase in resolved moisture fluxes at cloud base, primarily due to the increase in upward vertical velocities with resolution. The corresponding increase in downward vertical velocities with resolution are shown to stabilize the mean state, reducing the activity of the convection scheme and associated precipitation rates with increasing resolution. The feedback of the resolved vertical motion on the model physics indicates that the root cause of resolution sensitivity in CAM arises from the sensitivity of resolved dynamical modes to native grid resolution. Section 2 describes CAM6 and the details of the convergence experiment. Section 3 contains a thorough analysis of the CAM6 simulations and Section 4 provides some discussion and conclusions.

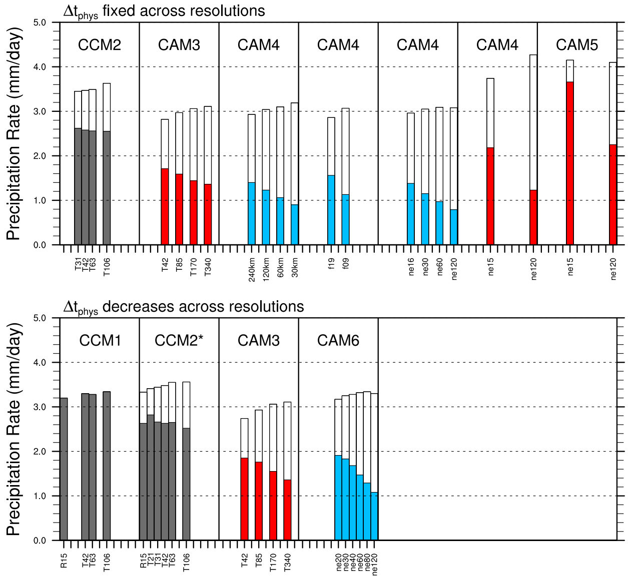

Figure 1. Bar-graph of the convective (solid) and stratiform (white) climatological precipitation rates in prior CAM/CCM convergence studies. Each window contains a single convergence experiment, with identical x-axis; the approximate grid resolution. Colors indicate the model configuration; January ensemble (black) and aqua-planet configurations with SST profiles $QOBS$ (blue) and $CNTL$ (red) in Neale and Hoskins (2000). Studies included in this figure are Kiehl and Williamson (1991) (CCM1), Williamson *et al.* (1995) (CCM2), Williamson (2008) (CAM3), Rauscher *et al.* (2013); Zarzycki *et al.* (2014); Herrington and Reed (2017) (CAM4), Zarzycki *et al.* (2014) (CAM5) and this study (CAM6). CCM2* refers to the modified parameter experiment of Williamson *et al.* (1995), where parameters vary with resolution to reduce the dependence of cloud fraction on resolution.

2. Methods

2.1. Dynamical Core

This study uses the spectral-element dynamical core option of Community Atmosphere Model (CAM-SE; Dennis *et al.* 2012), coupled with a mass conserving, semi-Lagrangian advection method for accelerated multi-tracer transport (CSLAM; Lauritzen *et al.* 2017), and dry-mass vertical coordinate with comprehensive treatment of moisture and energy (Lauritzen *et al.* 2018). The dry dynamics are solved using the high-order, momentum, mass and energy conserving spectral element method (Taylor and Fournier 2010), with the elements defined by a cubed-sphere grid. The notation for horizontal grid resolution is an 'ne' followed by the number of elements making up an edge of one cubed-sphere face, e.g., $ne30$. Hyper-viscous ∇^4 damping is applied to temperature, dry pressure thickness, rotational and divergent winds (Lauritzen *et al.* 2018). CSLAM tracer transport uses a finite volume grid constructed from the cubed-sphere of elements, and contains the same degrees of freedom as the dry dynamics.

2.2. Physical Parameterizations

The physics are evaluated on the finite-volume CSLAM grid, and the tendencies mapped back to the spectral element grid. The coupled system, referred to as CAM-SE-CSLAM, conserves energy, mass and preserves linear correlations between two reactive species to within machine precision (Herrington *et al.* 2018). A coarser physics grid, containing $\frac{5}{9}$ fewer degrees of freedom than the dynamical core grid is also available as part of the CAM-SE-CSLAM package (Herrington *et al.* 2019). This lower-resolution physics grid is used in this study, but only as a member of a perturbed parameter ensemble and not in the control convergence experiment. The dynamics time-step is subcycled within a longer physics time-step Δt_{phys}, and the temperature and momentum increments from the physics are divided by the

Table 1. Experimental design and global mean climatologies. Δx refers to the average equatorial grid-spacing.

Variable	$ne20$	$ne30$	$ne40$	$ne60$	$ne80$	$ne120$
Δx (km)	166.8	111.2	83.4	55.6	41.7	27.8
ν (m^4/s)	1.5×10^{15}	4.0×10^{14}	1.5×10^{14}	4.0×10^{13}	1.5×10^{13}	4.0×10^{12}
Δt_{phys} (s)	2700	1800	1350	900	675	450
Total Cloud Fraction	0.844	0.835	0.824	0.810	0.804	0.800
Total Precipitable Water (mm)	23.31	23.01	22.62	22.25	21.93	21.72
Convective Precipitation, P_c (mm/day)	1.91	1.83	1.68	1.47	1.29	1.08
Stratiform Precipitation, P_s (mm/day)	1.26	1.42	1.60	1.85	2.05	2.22

number of subcycles and added to the dynamical core at the beginning of each subcycle. The full moisture increment from the physics is applied only at the start of the first subcycle to conserve tracer mass ($ftype = 2$ option in Lauritzen and Williamson 2019).

The simulations use the CAM6 physics package. The Cloud Layers Unified by Binormals (CLUBB Golaz *et al.* 2002; Bogenschutz *et al.* 2013) is an assumed filtered density function (Germano 1992) high-order closure model that handles shallow convection, planetary boundary layer mixing and cloud macrophysics. The macrophyiscs are coupled with a two-moment bulk cloud microphysics scheme with prognostic precipitation (Gettelman *et al.* 2015), and microphysics are coupled with the three mode Modular Aerosol Model (Liu *et al.* 2012). The combined macrophysics/microphysics routines generate stratiform clouds and stratiform precipitation. Deep convection is parameterized using a quasi-equilibrium mass flux scheme (Zhang and McFarlane 1995) and an entraining plume calculation (referred to as the dilute convective available potential energy, or *dilute CAPE* hereafter; Raymond and Blyth 1992; Neale *et al.* 2008) is used as a convective trigger (convection occurs if dilute CAPE ≥ 70 J/kg), and for closing the mass fluxes in the cloud ensemble. The deep convection scheme also parameterizes convective momentum transport (Richter and Rasch 2008).

2.3. *Experimental Design*

The convergence experiment is performed in an aqua-planet configuration (Neale and Hoskins 2000; Medeiros *et al.* 2016), an all ocean planet with fixed, zonally symmetric sea surface temperatures modeled after present day Earth ($QOBS$ in Neale and Hoskins 2000). The aqua-planets are in a perpetual equinox, and aerosols are largely absent from the simulations. Each simulation is ran for one simulated year. Six different horizontal grids are used in this study, which are provided in Table 1. In addition to the six simulations used in the convergence experiment, an ensemble of 24 simulations containing different model parameters (e.g., using the lower resolution physics grid) and across different resolutions are ran for one year in order to increase confidence in assessing the resolution sensitivity in this study. All analyses exclude the first month of the simulations, which is sufficient to avoid the spin-up period; the model comes into global energy balance after about ten days (not shown). All calculations are performed on their native grids unless otherwise stated.

The horizontal hyper-viscosity operators ν vary with resolution after Herrington *et al.* (2019), also provided in Table 1. The values of ν are a factor 2.5 greater for divergence damping and are not shown. Δt_{phys} is chosen to scale with resolution, in proportion to the grid spacing,

$$\Delta t_{phys} = \Delta t_{phys,0} \times \frac{n_{e,0}}{ne}, \tag{2}$$

where $\Delta t_{phys,0}$ is taken to be the standard 1800 s used in CAM-SE-CSLAM for the standard climate resolution, $n_{e,0} = 30$ (equivalent to an average equatorial grid spacing $\Delta x = 111.2$km). This scaling was chosen to avoid large time-truncation errors in a rising moist bubble test (Appendix A in Herrington *et al.* 2019),

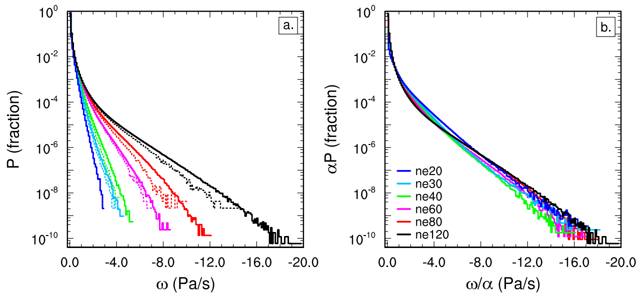

Figure 2. Probability density distribution of the upward vertical pressure velocities ω computed everywhere in the model from six-hourly output over the entirety of the year-long simulations. (a) Values on their native grid (solid) and values bilinearly remapped to the $ne20$ grid (dotted), (b) values on their native grid, scaled to the $ne120$ resolution using a power law exponent $n = -1$ in equation 1.

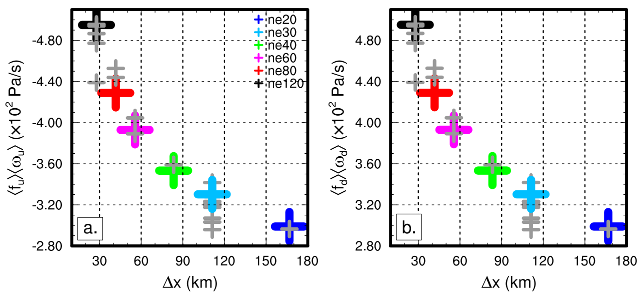

Figure 3. Components of the climatological, global mean vertical pressure velocity, (a) $\langle f_u \rangle \langle \omega_u \rangle$ and (b) $\langle f_d \rangle \langle \omega_d \rangle$. Grey crosses are for the 24 member perturbed parameter ensemble.

and it is understood that this choice of Δt_{phys} will likely lead to greater resolution sensitivity (Williamson 2008). The convective time-scale in the deep convection scheme is fixed at 3600 s in all simulations.

3. Results

Table 1 provides some globally averaged, climatological metrics for the CAM6 convergence experiment, commonly published in CAM/CCM convergence studies. Total precipitable water, total cloud fraction and deep convective precipitation rate decreases, while stratiform precipitation increases, monotonically with resolution (also shown in Figure 1). Resolution sensitivity in CAM6 is similar to all prior versions of the model.

3.1. *Vertical Velocities and Resolution*

The probability density function (PDF) of negative, or upward vertical pressure velocities ω in the aqua-planets is provided in Figure 2a. The magnitude of upward ω increases monotonically with resolution, with positive, or downward ω behaving similarly (not shown). This monotonic increase in the magnitude of ω is evident even after remapping all model output to a common grid ($ne20$; dotted curves in Figure 2a).

The PDF's may be scaled to the highest-resolution, $ne120$ grid through $\alpha P(\omega/\alpha)$, where $P(x)$ is the PDF and α the scale factor from equation 1 with Δx_0 set to the $ne120$ grid-spacing. Figure 2b shows the scaled PDF's for a power law exponent $n = -1$ in Δx. The scaled PDF's all collapse onto the high-resolution reference, indicating that the power-law exponent $n = -1$ explains to first-order the variation in vertical velocity with resolution as shown by the aqua-planet simulations.

Changes to the vertical velocity field can be further understood through decomposing the mass weighted vertical mean $\langle\omega\rangle$ into upward and downward components,

$$\langle\omega\rangle = \langle f_u\rangle \langle\omega_u\rangle + \langle f_d\rangle \langle\omega_d\rangle, \tag{3}$$

where $\langle f_x\rangle$ and $\langle\omega_x\rangle$ refers to the vertical mass fraction $\left(\frac{\int dp_x}{\int dp}, \text{ with pressure } p\right)$ and the x component of the mass weighted vertical mean of ω $\left(\frac{\int \omega_x dp_x}{\int dp_x}\right)$, respectively, subscript u refers to upward motion and d, downward motion.

The global mean, climatological components $\langle f_u\rangle \langle\omega_u\rangle$ and $\langle f_d\rangle \langle\omega_d\rangle$ are provided in Figure 3a,b for the aqua-planet simulations. The magnitude of both $\langle f_u\rangle \langle\omega_u\rangle$ and $\langle f_d\rangle \langle\omega_d\rangle$ increase monotonically with resolution, and are equal and opposite, which is a requirement of mass conservation in the model and a convenient check of the calculation. While $\langle f_d\rangle$ is about 25% larger than $\langle f_u\rangle$ in all simulations, the vertical mass fractions vary by only few percent with resolution, and so the monotonic behavior of $\langle f_x\rangle \langle\omega_x\rangle$ with resolution is primarily from variations in $\langle\omega_x\rangle$ (not shown).

3.2. *Vertical Velocities and Stratiform Precipitation*

Rauscher *et al.* (2016) proposed an approximate scaling for the total precipitation rate in models P_{tot}, proportional to the upward moisture flux through cloud base,

$$P_{tot} \approx -\frac{1}{g\rho_w}\omega q|_{cb} \tag{4}$$

where $\omega q|_{cb}$ refers to the product of ω and specific humidity q for ascending motion at cloud base, respectively, with $g = 9.80616$ m/s^2 the acceleration of gravity and $\rho_w = 1000$ kg/m^3 the density of rainwater used in CAM. O'Brien *et al.* (2016) deem this the "what goes up, must go down" model, highlighting the physically intuitive nature of the scaling, but note the scaling omits other potentially important processes, such as detrainment of cloudy updrafts into the environment or updrafts embedded within efficient circulations, with large gross moist stabilities.

Through approximating the cloud base as the 850 hPa level, equation 4 was found to provide a good fit to total precipitation rates in a regional model (Rauscher *et al.* 2016) and in the CAM-SE AGCM with CAM5 physics, across multiple resolutions (recall that CAM-SE is different from CAM-SE-CSLAM, used in this study; O'Brien *et al.* 2016). As noted by Rauscher *et al.* (2016), using only resolved quantities in equation 4 omits the sub-grid scale contribution to moisture fluxes, and so it is instructive to analyze the relative skill of this approximation for the individual components of P_{tot}, being the sum of stratiform P_s and parameterized deep convective P_c precipitation rates. Figure 4 shows the median P_c, P_s and P_{tot} conditioned on the 850 hPa resolved moisture flux scaling using 1 mm/day bins, in the CAM6 $ne30$ simulation. The figure shows that the moisture flux scaling is a good first-order approximation to the median total precipitation rate, and that the increase in precipitation rates with moisture flux is primarily from the stratiform precipitation scheme. The scaling is just as skillful for different resolutions (not shown; O'Brien *et al.* 2016) and so changes in stratiform precipitation rate with resolution can be understood through quantifying changes in resolved moisture fluxes with resolution.

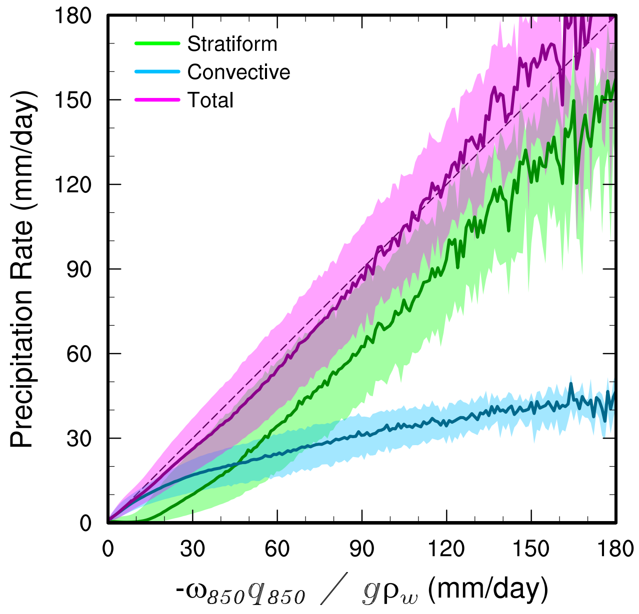

Figure 4. Precipitation rates vs. upward moisture flux at the 850 hPa level. Solid lines refer to median stratiform (green), convective (blue) and total (magenta) precipitation rates conditional on bins of the moisture flux, and shaded regions refer to the conditional interquartile ranges.

Table 2. Fractional contribution of latitude bands $\pm 10°$ and $\pm 15°$ to changes in global mean stratiform and parameterized convective precipitation with resolution. The grid headers refer to differences with respect to the next lowest grid resolution, e.g., $ne30 = ne30 - ne20$, $ne40 = ne40 - ne30$, etc... All differences are computed after conservative remapping to a common $ne20$ grid.

Variable	$ne30$	$ne40$	$ne60$	$ne80$	$ne120$
$\pm 10°$ (17.6% of global area)					
Convective Precipitation, P_c	-0.58	0.62	0.66	0.72	0.70
Stratiform Precipitation, P_s	0.55	0.63	0.69	0.67	0.41
$\pm 15°$ (25.8% of global area)					
Convective Precipitation, P_c	0.22	0.75	0.73	0.79	0.72
Stratiform Precipitation, P_s	0.46	0.64	0.71	0.70	0.49

To unravel the contributions of changes in ω and q at the 850 hPa level, ω_{850} and q_{850}, to the increase in global mean, climatological stratiform precipitation rates $\overline{P_s}$, $\overline{P_s}$ is decomposed in ω_{850} and q_{850} space following Terai *et al.* (2018). Table 2 shows the fractional contribution of deep tropical belts to the global mean change in stratiform precipitation with resolution. The table indicates that roughly a majority $(45 - 70\%)$ of the increase in stratiform precipitation with resolution is from changes within the $\pm 15°$ latitude band, and so the moisture flux decomposition is restricted to this region to simplify the analysis; $\overline{P_s}$ is redefined as the average over $\pm 15°$ latitude.

$\overline{P_s}$ can be expressed as the double sum of the product of the time mean magnitude M_s and time mean spatial frequency f_s, over ω_{850} and q_{850} space,

$$\overline{P_s} = \sum_i \sum_j f_s\left(\omega_i, q_j\right) M_s\left(\omega_i, q_j\right) \tag{5}$$

where the subscript 850 is dropped from ω and q for brevity. f_s is a measure of the occurrence of a particular combination $\left(\omega_i, q_j\right)$ in a simulation, and M_s the mean stratiform precipitation rate associated with the combination $\left(\omega_i, q_j\right)$. Their product $f_s M_s$ is then the contribution of the combination $\left(\omega_i, q_j\right)$ to $\overline{P_s}$.

Figure 5 shows plots of the terms M_s and $f_s M_s$ for all resolutions. The plots are computed using 6-hourly instantaneous output of ω_{850} and q_{850}, with 0.05 Pa/s and 0.4 g/kg bin widths, respectively. Bins in $\left(\omega_i, q_j\right)$ space with $f_s < 1 \times 10^{-5}$ are masked out, which is a somewhat arbitrary, but reasonable cut-off for a bins' contribution to $\overline{P_s}$. The M_s plots (left column) show that larger magnitude ω_{850} correspond to larger magnitude stratiform precipitation rates, while the impact of changing q_{850} on M_s is less clear. The changes in M_s with resolution are subtle, while the changes in f_s with resolution are large (not shown). The changes to f_s can be inferred from the larger space of (ω_i, q_j) plotted at higher resolutions, indicating that larger magnitude ω_{850} values are occurring more frequently at higher resolutions, above the cutoff for plotting. The $f_s M_s$ plots (right column) clearly shows that larger magnitude ω_{850}, and therefore larger magnitude stratiform precipitation rates, are contributing to the increase in $\overline{P_s}$ with resolution. In contrast, smaller magnitude ω_{850} and hence smaller stratiform precipitation rates contribute less and less to $\overline{P_s}$ with increasing resolution.

3.3. *Vertical Velocities and Deep Convective Precipitation*

While the increase in magnitude of vertical velocities with resolution clearly drives an increase in moisture fluxes and stratiform precipitation rates with resolution, it is not clear why there is a reduction in parameterized deep convective precipitation rates with resolution, in all versions of the model (Figure 1). Curiously though, there is an excellent negative correlation (Pearson's R-value = 0.99, N = 27) between the global mean, climatological $\langle f_d \rangle \langle \omega_d \rangle$ and a measure of the activity of the Zhang and McFarlane (1995) deep convection scheme (referred to as the *ZM scheme* hereafter), global mean, climatological $FREQZM$ (Figure 6). At any grid-point and time-step, $FREQZM$ is a binary variable: 1 if the ZM scheme is active, 0 if it is not. Time mean $FREQZM$ is therefore the fraction of the model time that the ZM scheme is triggered, i.e., dilute CAPE exceeds ≥ 70 J/kg. The regression indicates that model simulations with greater subsidence also have less convective activity.

Figure 7a,b, shows the zonal mean variations in $\langle f_d \rangle \langle \omega_d \rangle$ and $FREQZM$ in the convergence experiment. $FREQZM$ is largest in the $\pm 10^\circ$ latitude region, within the Inter-Tropical Convergence Zone (ITCZ), and rapidly decreasing polewards into the subtropics. $\langle f_d \rangle \langle \omega_d \rangle$ increases away from the ITCZ region and reaches a maximum at the poleward limit of the Hadley Cell. The increase (decrease) in $\langle f_d \rangle \langle \omega_d \rangle$ ($FREQZM$) with resolution is to first-order, independent of latitude.

To further understand the relationship between subsidence and activity of the ZM scheme, a logistic regression between $\langle f_d \rangle \langle \omega_d \rangle$ and $FREQZM$ is performed for each grid column within each of the simulations. Logistic regression uses an iterative method to fit a continuous variable predictor, x to a binary predictand p using the exponential (Wilks 2011),

$$p = \frac{exp[b_0 + b_1 x]}{1 + exp[b_0 + b_1 x]}, \tag{6}$$

where b_0 and b_1 are the shape parameters of the exponential. The predictor is the instantaneous $\langle f_d \rangle \langle \omega_d \rangle$ of a grid column, and the predictand the binary $FREQZM$. The assumption is then that subsidence is the independent variable, which is reasonable considering the environment of subsiding regions is generally more stable than its surroundings, and the ZM scheme is modulated by the dilute CAPE stability calculation. Grid column regressions that are statistically significant at the 95% level using a log-likelihood test (Wilks 2011) are retained for analysis. Since the aqua-planets have zonally symmetric boundary conditions, there is a zonally varying structure in the goodness of fit (R-value) and shape parameter b_1 (Figure 7c,d).

The zonal mean R-values indicate the greatest goodness of fit in the $\pm 10^\circ$ latitude band, hereafter referred to as the deep tropics. In this region, the shape parameter b_1 is large and

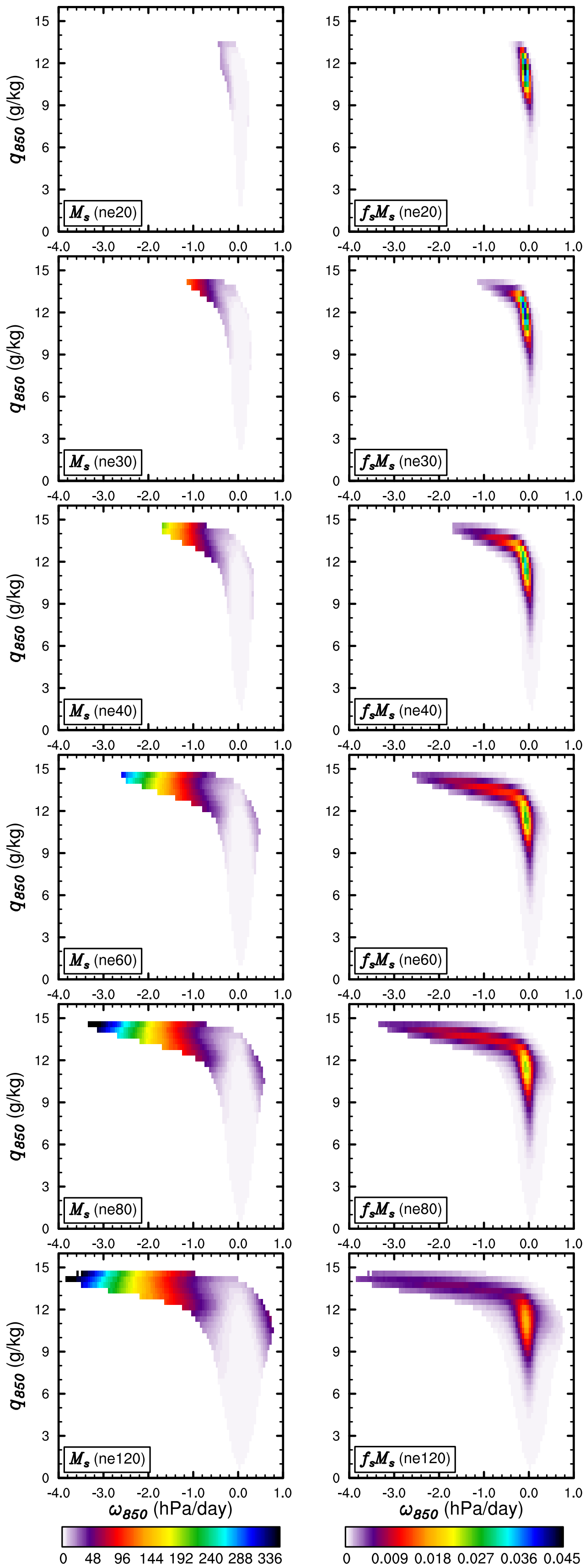

Figure 5. Decomposition of the climatological stratiform precipitation rates, averaged over the $\pm 15^\circ$ latitude band into ω_{850} and q_{850} environmental conditions. Left column shows the time mean magnitude term $M(\omega_i, q_j)$ and the right column is the magnitude term multiplied by the space-time frequency term $f(\omega_i, q_j) M(\omega_i, q_j)$. Integrals over fM gives the climatological, area averaged stratiform precipitation rate. Panel labels denote the grid resolution of the model run.

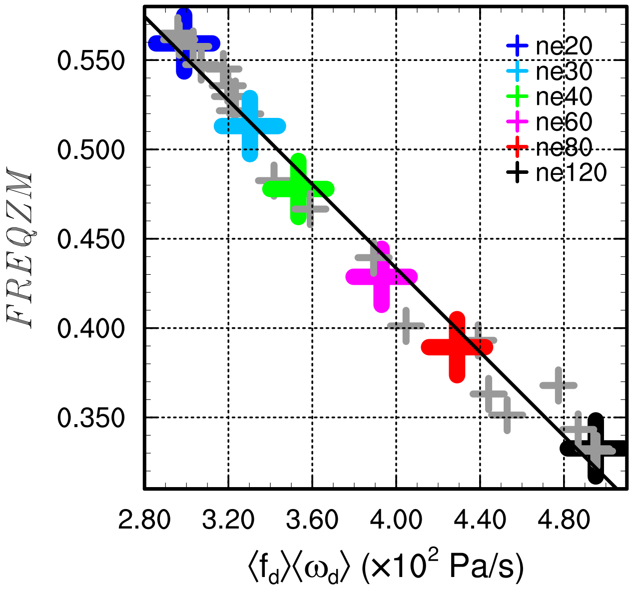

Figure 6. Scatter plot of global mean, climatological $\langle f_d \rangle \langle \omega_d \rangle$ and $FREQZM$, and the fitted linear regression which has a Pearson's R-value = 0.99, using all 27 simulations. Grey crosses are for the 24 member perturbed parameter ensemble runs.

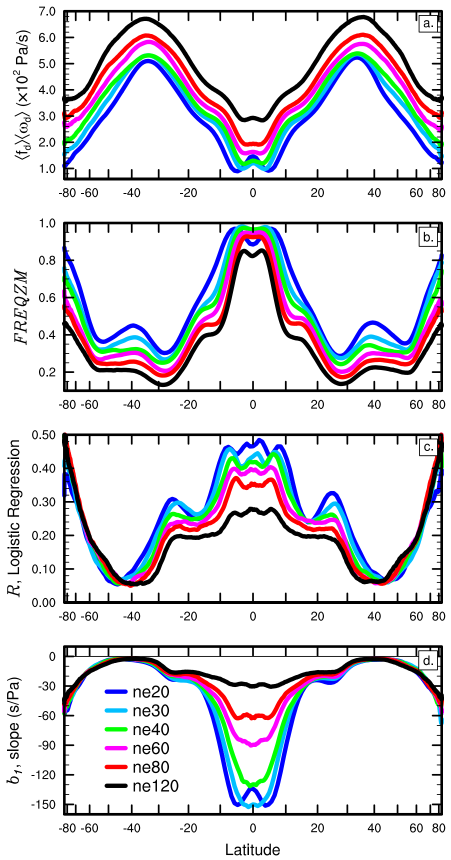

Figure 7. Zonal mean (a) climatological $\langle f_d \rangle \langle \omega_d \rangle$ and (b) climatological $FREQZM$. Zonal mean (c) R-values and (d) the shape parameter b_1 in the logistic regression.

negative (Figure 7d), consistent with the idea that subsiding motion stabilizes the environment and actively depresses dilute CAPE and the activity of the ZM scheme in the simulations. The shape parameter becomes less negative in the deep tropics with resolution, likely due to the greater magnitude $\langle f_d \rangle \langle \omega_d \rangle$ with resolution, which requires a lower b_1 to predict the binary $FREQZM$. The R-values generally decrease with resolution indicating that there is degradation in the relationship with resolution. The logistic regression is less skillful in the subtropics, with skill declining even further in the mid-latitudes irregardless of resolution (Figure 7c).

3.3.1. Deep Tropics

Table 2 indicates that a majority ($60 - 70\%$) of the reduction in convective precipitation with resolution is from changes within the deep tropics (except in going from $ne20$ to $ne30$, where convective precipitation rates increase, in part due to a wide double-ITCZ in the $ne20$ run that spans outside of $\pm 10°$ latitude, but which is contained within $\pm 10°$ latitude in the $ne30$ run). Expanding the latitude boundaries marginally to $\pm 15°$, roughly 75% of the changes in convective precipitation with resolution occurs in this region (again, ignoring $ne30 - ne20$; Table 2). This trend reflects changes in the partitioning of the ITCZ from convective to stratiform precipitation with resolution.

The large reduction in convective precipitation with resolution in the deep tropics also happens to be the region where the logistic regression indicates that subsiding motion is most skillful at depressing the activity of the convection scheme. But the change in $FREQZM$ in the deep tropics with resolution is not substantially different from any other region (Figure 7b), such as the midlatitudes where the logistic regression indicates a poor relationship between subsidence and $FREQZM$ (Figure 7c). The deep tropics is then only unique for its substantially larger change in ZM precipitation per change in $FREQZM$ with resolution.

To characterize the changes to dilute CAPE of subsiding regions in the deep tropics with resolution, temperature and moisture profiles are conditionally sampled depending on whether $\langle \omega \rangle$ is positive or negative, indicating predominantly subsiding or ascending grid columns. The time mean temperature and moisture profiles of subsiding and ascending regions are then used to compute the dilute CAPE used in the ZM scheme, offline. Figure 8a shows the dilute CAPE values associated with mean conditions for ascending, descending and all grid columns in the deep tropics, with resolution. Ascending regions are associated with larger values of dilute CAPE (> 180 J/kg) relative to subsiding regions (< 110 J/kg), and the dilute CAPE in both regimes decreases monotonically with resolution.

Figure 9 shows the time mean temperature and specific humidity profiles of subsiding grid cells in the deep tropics, expressed as anomalies from the mean temperature and specific humidity of the entire deep tropics. The mean profiles of subsiding regions have an anomalous warming layer in the $600 - 800$ hPa layer and an anomalous moisture deficit throughout the entire column. This warming and drying pattern is consistent with the effects of subsidence, whose motion adiabatically warms the environment while simultaneously advecting drier conditions aloft, downward. Both warming and drying the environment oppose the growth of dilute CAPE through reducing parcel buoyancy; warming the environment relative to the temperature of rising air parcels reduces parcel buoyancy (Zhang 2002), and mixing drier environmental air into rising air parcels reduces the moisture available to warm parcels through latent heating (Raymond and Blyth 1992).

The large spread in dilute CAPE between ascending/descending regions is crucial for maintaining the relationship shown by the logistic regression, since the much smaller values of dilute CAPE of subsiding grid columns is required to depress dilute CAPE below the threshold for convection. To unravel the contributions of warming and drying shown in Figure 9 to the large spread in dilute CAPE between the two regimes, dilute CAPE is recomputed using the mean specific humidity of ascending/descending regions in the deep tropics, but setting the

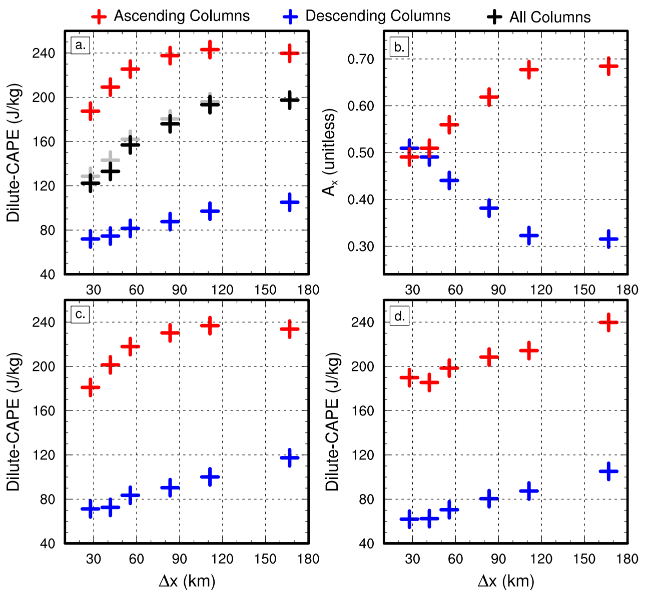

Figure 8. (a) Dilute CAPE computed from time mean temperature and moisture profiles of ascending (red), subsiding (blue) and all grid columns (black) in the deep tropics ($\pm 10°$ latitude), and (b) space-time weights of ascending (red) and descending (blue) grid columns in the deep tropics. (c) Dilute CAPE computed for ascending/descending grid columns, but using the mean temperature profile for the entire deep tropics, and (d) Dilute CAPE for ascending/descending regions but fixing moisture to the $ne20$ profile. Grey crosses in (a) are dilute CAPE derived from the sum of the products of space-time weights with the dilute CAPE values of ascending/descending grid columns.

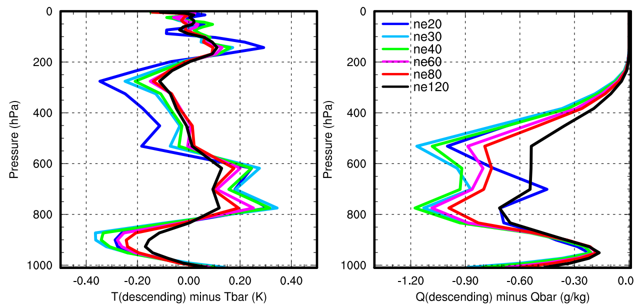

Figure 9. Time mean (a) temperature and (b) specific humidity profiles of subsiding grid cells in the deep tropics ($\pm 10°$ latitude) in the convergence experiment, presented as anomalies from the mean temperature and specific humidity of the entire deep tropics in each simulation.

temperature profile to the mean profile for the entire deep tropics. Figure 8c shows this influence of changing moisture on dilute CAPE, which to first order, explains the large spread in dilute CAPE between the ascending/descending regions in the deep tropics. Temperature differences between ascending/descending regimes has a smaller, second order influence on the spread in dilute CAPE (not shown).

The space-time weights associated with ascending and descending grid columns in the deep tropics vary drastically with resolution (Figure 8b). The subsiding (ascending) space-time weights change from 0.32 (0.68) in the $ne20$ run, monotonically increasing (decreasing) with resolution to 0.51 (0.49) in the $ne120$ run. The increasing occurrence of stable, subsiding grid columns accounts for about half of the changes in dilute CAPE in the deep tropics with resolution, the other half being due to the systematic reduction in dilute CAPE for both ascending and descending regions (Figure 8a). This breakdown is straightforward to compute since the sum of the products of the space-time fractions with their associated ascending/descending dilute CAPE values approximate the dilute CAPE computed from the mean temperature/moisture

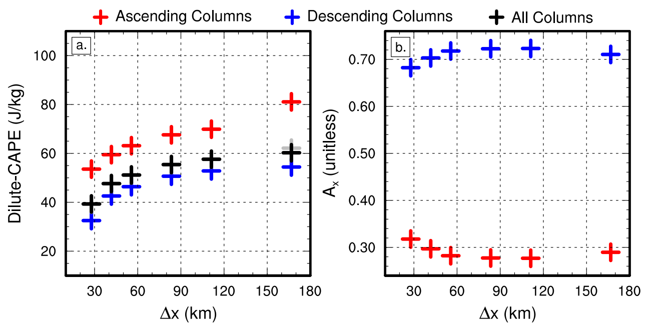

Figure 10. (a) Dilute CAPE computed from time mean temperature and moisture profiles of ascending (red), subsiding (blue) and all grid columns (black) in the subtropics ($\pm(10° - 30°)$ latitude bands), and (b) space-time weights of ascending (red) and descending (blue) grid columns in the subtropics. Grey crosses in (a) are dilute CAPE derived from the sum of the products of space-time weights with the dilute CAPE values of ascending/descending grid columns.

profiles over the entire deep tropics quite well (compare black and grey crosses in Figure 8a).

To isolate the relative importance of temperature or moisture on the systematic reduction in dilute CAPE with resolution for both ascending/descending regimes, dilute CAPE is recomputed for all resolutions, but through fixing the moisture profiles to the lowest resolution $ne20$ profile, and then through fixing only the temperature to the $ne20$ profile. Figure 8d shows the influence of changing temperature profile with resolution, with moisture fixed to the $ne20$ profile, on dilute CAPE of ascending/descending grid columns, and illustrates that the systematic reduction in dilute CAPE with resolution in both regimes is primarily from changes to the temperature field. Moisture changes with resolution do not contribute to the reduction in dilute CAPE with resolution, with the exception that the 20 J/kg reduction in dilute CAPE of ascending regions between the $ne80$ and $ne120$ runs (Figure 8a) is entirely due to changes in moisture (not shown).

3.3.2. *Subtropics*

Figure 10a shows the dilute CAPE values computed from mean temperature and moisture of subsiding and ascending regions in the $\pm(10° - 30°)$ latitude bands, hereafter referred to as the subtropics. The spread in dilute CAPE between ascending and descending grid columns is much smaller than for the deep tropics (Figure 8a), and their dilute CAPE values vary much less with resolution ($\sim$ 20 J/kg, compared with $\sim$ 80 J/kg across all resolutions in the deep tropics). Through recomputing dilute CAPE and fixing the temperature or moisture profiles to $ne20$ values, the reduction in dilute CAPE with resolution is attributed to both temperature and moisture, but as in the deep tropics, temperature changes have a larger influence (not shown). This analysis suggests that increasing subsidence with resolution (Figure 7a) increases the stability of the mean state, since both ascending/descending regimes become more stable with resolution, and reducing climatological $FREQZM$ (Figure 7b) despite the poor relationship between instantaneous subsidence and $FREQZM$ in the subtropics, as shown by the logistic regression (Figure 7c).

It is the lack of spread in dilute CAPE between ascending/descending regions that explains the declining skill in the logistic regression in the subtropics (Figure 7c). Without a strong dependence of dilute CAPE on ascending/descending regimes, subsidence is not a very skillful predictor of depressing dilute CAPE below the threshold for convection. In contrast to the deep tropics, there is also no significant changes to the occurrence of subsiding grid columns with resolution; space-time weights of ascending/descending motion are more-or-less invariant with resolution (Figure 10b).

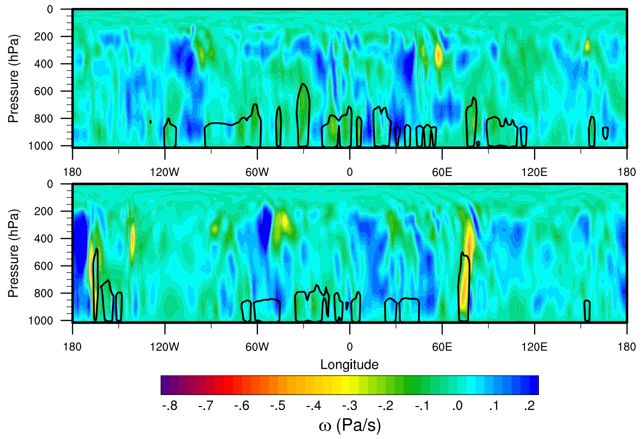

Figure 11. (a,b) Two snapshots of ω for a longitude-pressure transect at $\sim 18^\circ$ latitude in the $ne30$ simulation, overlain by the 0.0075 kg/m^2/s contour of the ZM mass flux delineating the region where the ZM scheme is active.

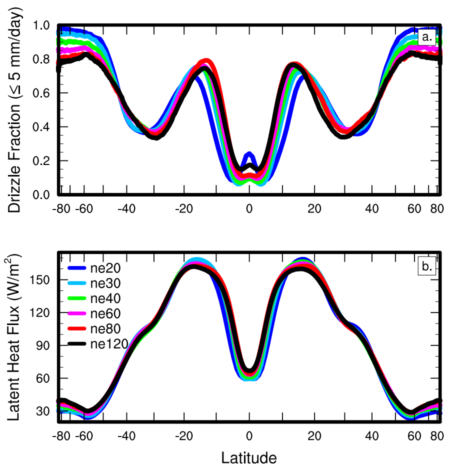

Figure 12. Climatological zonal mean (a) drizzle fraction and (b) surface latent heat fluxes in the convergence experiment. Drizzle fraction is defined as sum convective precipitation rates ≤ 5 mm/day divided by the sum of all convective precipitation rates, computed from 6-hourly instantaneous fields over the duration of the simulation.

To understand why dilute CAPE is less sensitive to subsidence in the subtropics, Figure 11 shows two snapshots of ω in the longitude-pressure plane at $\sim 18^\circ$ latitude in the $ne30$ simulations, overlain by an isoline delineating where the ZM mass fluxes are quite active. The ZM mass fluxes typically only extend up to about the 800 hPa level in this region, which often occurs with appreciable subsiding motion aloft. Though properly a deep convection scheme, the ZM scheme is acting as a shallow convection scheme in this region (Terai *et al.* 2016). This shallow convection regime tends to produce light rain, or drizzle, which is a common bias in AGCMs (Dai 2006). Figure 12a shows the fraction of ZM precipitation ≤ 5 mm/day in the simulations, which stubbornly persists at $\sim 70\%$ in the $\pm(10^\circ - 20^\circ)$ latitude bands, irrespective of resolution.

In the $\pm(10^\circ - 20^\circ)$ latitude bands there are opposing influences on dilute CAPE; a global maximum in surface latent heat fluxes (Figure 12b), influencing the thermodynamic state of boundary layer parcels and increasing dilute CAPE from below (Zhang 2002), and increasing subsidence (Figure 7a), which opposes dilute CAPE from above. The shallow convection regime of the ZM scheme is likely a result of these two opposing influences on dilute CAPE, with large latent heat fluxes increasing dilute CAPE above the threshold for convection, but with subsidence restricting dilute CAPE from becoming much larger than this threshold. This interpretation is supported by the logistic regression, which shows a local minimum in goodness-of-fit in the $\pm(10^\circ - 20^\circ)$ latitude region (Figure 7c), indicating that it is particularly difficult for subsiding motion to depress dilute CAPE below the threshold for convection where the surface latent heat fluxes are large.

4. Discussion and conclusions

Establishing a complete understanding of resolution sensitivity in atmospheric general circulation models (AGCMs) is crucial, since inevitable responses to native grid resolution cannot be ignored in the pursuit of physical parameterizations compatible with the highly flexible grid structures now being used to maximize efficiency on modern day supercomputers (i.e., scale-aware physics). This study analyzes a convergence experiment in an aqua-planet configuration using the Community Atmosphere Model (CAM), with the spectral-element dynamical core option coupled to the accelerated multi-tracer transport scheme (CAM-SE-CSLAM), and version 6 physics (CAM6), in order to understand longstanding convergence issues that have persisted within the CAM lineage since its inception (see Figure 1). As with most versions of CAM, in CAM6 the atmosphere becomes drier and less cloudy with increasing resolution, and parameterized convective precipitation decreases while stratiform precipitation increases with resolution. Prior studies have established that the drying and reduction in cloudiness with resolution is a result of increases in the magnitude of vertical velocities with resolution, which more efficiently advects dry air aloft, downward (Kiehl and Williamson 1991; Williamson *et al.* 1995; Herrington and Reed 2017). This study aims to then understand why and how vertical velocities change with resolution, and why convective precipitation decreases at the expense of stratiform precipitation with increasing resolution.

The vertical velocities are found to fit a power law scaling Δx^n with Δx the grid spacing and $n = -1$. The $n = -1$ exponent is derived from a scale analysis of the Poisson equation, indicating that pressure gradients scale like the inverse of the horizontal scale of buoyancy perturbations, D^{-1}, driving convergence into the air column and the vertical velocities also scale like D^{-1}. It has been previously shown that D is set by stratiform cloud formation, which collapse to the smallest resolvable feature in the model (Herrington and Reed 2018), the effective resolution (Skamarock 2011), and so $D \propto \Delta x$ giving $n = -1$. This scaling is consistent with studies describing the resolution sensitivity of large-eddy simulations, which use similar physical arguments, but adapted for non-hydrostatic scales (Weisman *et al.* 1997; Pauluis and Garner 2006; Jeevanjee and Romps 2016).

The $n = -1$ power law scaling is potentially in conflict with the scaling proposed by Rauscher *et al.* (2016), $n = h - 1$, with h being half the exponent of the second-order structure function Δx^{2h} of the horizontal wind. Rauscher *et al.* (2016) propose that since the $h = \frac{1}{3}$ is supported by observations, it is an emergent constraint for $n = -\frac{2}{3}$. This is an intriguing proposal and the authors don't seek to dismiss its potential value. But it is suggested that the overwhelming support for the $h = \frac{1}{3}$ exponent in the second-order structure function is only relevant for horizontal scales on the order of 100 km and less (Lindborg 1999; Cho and Lindborg 2001), which is only marginally resolved in the highest resolution simulation $\Delta x = 27.8$ km ($ne120$), and CAM-SE-CSLAM has an effective resolution in the range of $5 - 10\Delta x$ (Herrington *et al.* 2019). The nonexistence of $h = \frac{1}{3}$ in the $\Delta x = 27.8$ km simulation is verified through analyzing the slope of the kinetic energy spectrum $-\beta$, which is in duality with the second-order structure function through the Weiner–Khinchine theorem. For $h = \frac{1}{3}$, $\beta = \frac{5}{3}$, which is shallower than the slope

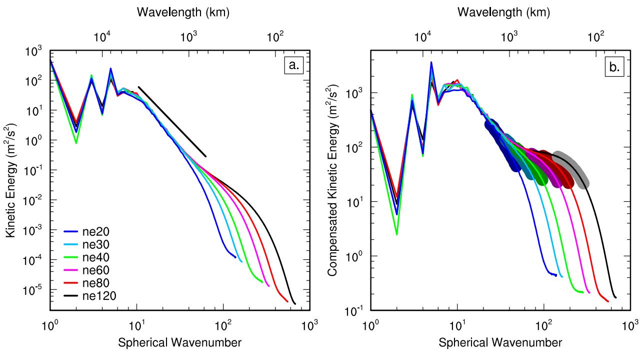

Figure 13. (a) Kinetic energy spectrum and (b) compensated kinetic energy spectrum at the 200 hPa level in the simulations. The diagonal black line in (a) is a reference spectrum with a -3 slope. Compensated kinetic energy spectrum refers to the kinetic energy spectrum multiplied by $n^{-\frac{5}{3}}$, with spherical wavenumber n, so that horizontal lines indicate a spectrum with a $-\frac{5}{3}$ slope. In (b), thick "caterpillars" are overlain on the portion of each spectrum pertaining to the $5-10\Delta x$ effective resolution of the model.

near where the spectrum approaches the effective resolution, for all grid resolutions (Figure 13). There is however, a progressive shoaling of the slope $-\beta$ with increasing resolution (Figure 13b). This suggests a transition towards the $-\frac{5}{3}$ slope in the model, but seeing this process through would require running the model at higher resolutions than considered in this study.

An increase in resolved moisture fluxes through cloud base occurs with increasing resolution, and balanced by an increase in stratiform precipitation rates. Through decomposing the stratiform precipitation into the components of the moisture flux, it is shown that the increase in stratiform precipitation rates with resolution is primarily due to the increase in resolved mass fluxes arising from the increase in resolved vertical velocities with resolution. At higher resolutions, larger stratiform precipitation rates increasingly contribute to the increase in climatological stratiform precipitation rate, with smaller magnitude precipitation rates contributing less. The increasing occurrence of larger magnitude vertical velocities and stratiform precipitation rates at higher resolution is at odds with a similar analysis by Terai *et al.* (2018) using a similar model. The authors suggests that their use of daily averaged fields obscured the covariance between vertical velocity and moisture (i.e., moisture flux) and complicated their calculation.

A strong negative correlation is discovered between the climatological, global mean activity of the Zhang and McFarlane (1995) deep convection scheme (ZM scheme) and global mean subsiding motion in the simulations. Since the ZM scheme is modulated by an entraining plume calculation, referred to as the dilute convective available potential energy (dilute CAPE), the authors sought to understand the influence of subsidence on dilute CAPE. In the deep tropics ($\pm 10^\circ$ latitude), subsiding regions have much smaller dilute CAPE values compared to ascending regions due to the influence of the drier subsiding environment on dilute CAPE. With increasing resolution and in the deep tropics, the occurrence of subsiding motion increases dramatically and at the expense of ascending motion, and the activity of the the ZM scheme decreases overall. This is consistent with the Δx^{-1} scaling of the vertical velocities, e.g., a doubling of resolution can generate the same upward mass flux in just half the area. The increased efficiency of upward mass fluxes with resolution suggests that the occurrence of ascending motion can decrease with resolution while still maintaining statistical equilibrium with the large-scale forcing.

In addition to the change in balance of ascending/descending motion in the deep tropics with resolution, temperature and moisture profiles show a decrease in dilute CAPE for both ascending/descending regimes with increasing resolution. This reduction in background dilute CAPE is not confined to the deep tropics, but is also evident from the dilute CAPE derived from the time mean temperature and moisture profiles everywhere in the model (not shown) and is in large part the reason for the global mean reduction in activity in the ZM scheme with resolution. A sensitivity analysis of the dilute CAPE calculation indicates that this change in background stability is primarily a result of temperature changes with resolution. Temperature profiles become more stable with increasing resolution, likely due to an increase in adiabatic warming due to the increase in subsidence with resolution.

Subsidence warming falls out of the component of the dilute CAPE budget due to the advection of dry static energy and moisture by the environment, commonly referred to as dynamic CAPE (DCAPE; Xie and Zhang 2000; Zhang 2002). Subsidence warming is represented in the DCAPE budget as negative the vertical advection of dry static energy term, since warming the environment reduces DCAPE, and simplifies to $\frac{w}{c_{pd}}\frac{\partial gz}{\partial z}=\frac{g}{c_{pd}}w$, directly proportional to the vertical velocity w by the factor $\frac{g}{c_{pd}}$, with g the acceleration of gravity and c_{pd} the specific heat capacity of dry air (F. Song, personal communication). The magnitude of negative, or downward, w increases everywhere in the model with increasing resolution, opposing the growth of dilute CAPE and reducing the activity of the ZM scheme with increasing resolution.

The subtropics ($\pm(10^\circ-30^\circ)$ latitude) are uniquely less sensitive to subsiding motion. This is likely due to the the large, global maximum in surface latent heat fluxes in the subtropics, which increases dilute CAPE above the threshold for convection, but which is restricted from growing much larger due to substantial subsiding motion aloft. These opposing influences result in small values of dilute CAPE, and the ZM scheme acts more like a shallow convection scheme, producing light precipitation or drizzle, irrespective of resolution.

AGCMs are known to suffer from an excess of drizzle relative to observations (Dai 2006). Xie *et al.* (2019) recently proposed a new convective trigger for the ZM scheme that the authors suggest may alleviate the excess drizzle bias in CAM. As with the ZM scheme used in this study, dilute CAPE must exceed a threshold for convection to occur, but Xie *et al.* (2019) also require DCAPE to be positive. Based on the analysis in this study, and the strong connection between vertical velocities and DCAPE reported in Song and Zhang (2018), it is reasonable to speculate that DCAPE is often negative in drizzling regions, and the Xie *et al.* (2019) trigger would not allow for convection to occur. The authors suggest that this trigger be explored as a means to mitigate the drizzling bias in future versions of CAM.

This study argues that the sensitivity of parameterized convection and stratiform precipitation rates to resolution are a response to the increase in magnitude of vertical velocities with resolution. This is essentially the hypothesis put forth by Herrington and Reed (2017) to explain resolution sensitivity, that increased vertical velocities with resolution interacts with other model components, steering the model towards a new mean state. Here, those interactions are documented explicitly. Resolution sensitivity therefore arises from the relationship between vertical velocities and resolution, a well-known scale dependency of the equations of motion (Orlanski 1981). This scale dependency needs to be addressed in the pursuit of scale-aware physics.

Acknowledgement

Funding support for this work was in part provided by the U.S. Department of Energy Office of Science (DE-SC0019459) and the National Science Foundation (AGS1648629 and AGS1830729). Computing and data storage resources, including the Cheyenne supercomputer (doi:10.5065/D6RX99HX), were provided by the Computational and Information Systems Laboratory (CISL) at the National Center for Atmospheric Research (NCAR). Herrington would like to thank Dr. Sultan Hameed for his assistance with the statistical analysis used in this study.

References

Arakawa A, Wu CM. 2013. A unified representation of deep moist convection in numerical modeling of the atmosphere. part i. *Journal of the Atmospheric Sciences* **70**(7): 1977–1992.

Bogenschutz PA, Gettelman A, Morrison H, Larson VE, Craig C, Schanen DP. 2013. Higher-order turbulence closure and its impact on climate simulations in the community atmosphere model. *Journal of Climate* **26**(23): 9655–9676.

Cho JY, Lindborg E. 2001. Horizontal velocity structure functions in the upper troposphere and lower stratosphere: 1. observations. *Journal of Geophysical Research: Atmospheres* **106**(D10): 10 223–10 232.

Cho JY, Zhu Y, Newell RE, Anderson BE, Barrick JD, Gregory GL, Sachse GW, Carroll MA, Albercook GM. 1999. Horizontal wavenumber spectra of winds, temperature, and trace gases during the pacific exploratory missions: 1. climatology. *Journal of Geophysical Research: Atmospheres* **104**(D5): 5697–5716.

Dai A. 2006. Precipitation characteristics in eighteen coupled climate models. *Journal of Climate* **19**(18): 4605–4630.

Davis A, Marshak A, Wiscombe W, Cahalan R. 1996. Scale invariance of liquid water distributions in marine stratocumulus. part i: Spectral properties and stationarity issues. *Journal of the atmospheric sciences* **53**(11): 1538–1558.

Dennis JM, Edwards J, Evans KJ, Guba O, Lauritzen PH, Mirin AA, St-Cyr A, Taylor MA, Worley PH. 2012. CAM-SE: A scalable spectral element dynamical core for the Community Atmosphere Model. *Int. J. High. Perform. C.* **26**(1): 74–89, doi:10.1177/1094342011428142, URL http://hpc.sagepub.com/content/26/1/74.abstract.

Donner LJ, O'Brien TA, Rieger D, Vogel B, Cooke WF. 2016. Are atmospheric updrafts a key to unlocking climate forcing and sensitivity? *Atmospheric Chemistry and Physics* **16**(20): 12 983–12 992.

Germano M. 1992. Turbulence: the filtering approach. *Journal of Fluid Mechanics* **238**: 325–336.

Gettelman A, Morrison H, Santos S, Bogenschutz P, Caldwell P. 2015. Advanced two-moment bulk microphysics for global models. part ii: Global model solutions and aerosol–cloud interactions. *Journal of Climate* **28**(3): 1288–1307.

Golaz JC, Larson VE, Cotton WR. 2002. A pdf-based model for boundary layer clouds. part i: Method and model description. *Journal of the Atmospheric Sciences* **59**(24): 3540–3551, doi:10.1175/1520-0469(2002)059⟨3540:apbmfb⟩2.0.co;2.

Harris LM, Lin SJ, Tu C. 2016. High-resolution climate simulations using gfdl hiram with a stretched global grid. *Journal of Climate* **29**(11): 4293–4314, doi:10.1175/jcli-d-15-0389.1.

Herrington A, Lauritzen P, Taylor MA, Goldhaber S, Eaton BE, Bacmeister J, Reed K, Ullrich P. 2018. Physics-dynamics coupling with element-based high-order galerkin methods: quasi equal-area physics grid. *Mon. Wea. Rev.* **47**: 69–84, doi:10.1175/MWR-D-18-0136.1.

Herrington A, Reed K. 2018. An idealized test of the response of the community atmosphere model to near-grid-scale forcing across hydrostatic resolutions. *J. Adv. Model. Earth Syst.* **10**(2): 560–575.

Herrington AR, Lauritzen PH, Reed KA, Goldhaber S, Eaton BE. 2019. Exploring a lower resolution physics grid in cam-se-cslam. *Journal of Advances in Modeling Earth Systems* **11**.

Herrington AR, Reed KA. 2017. An explanation for the sensitivity of the mean state of the community atmosphere model to horizontal resolution on aquaplanets. *J. Climate* **30**(13): 4781–4797, doi:10.1175/jcli-d-16-0069.1, URL http://dx.doi.org/10.1175/jcli-d-16-0069.1.

Jeevanjee N. 2017. Vertical velocity in the gray zone. *Journal of Advances in Modeling Earth Systems* **9**(6): 2304–2316, doi:10.1002/2017MS001059.

Jeevanjee N, Romps DM. 2016. Effective buoyancy at the surface and aloft. *Quart. J. Roy. Meteor. Soc.* **142**(695): 811–820.

Kiehl J, Williamson D. 1991. Dependence of cloud amount on horizontal resolution in the national center for atmospheric research community climate model. *Journal of Geophysical Research: Atmospheres* **96**(D6): 10 955–10 980.

Lauritzen PH, Nair R, Herrington A, Callaghan P, Goldhaber S, Dennis J, Bacmeister JT, Eaton B, Zarzycki C, Taylor MA, Gettelman A, Neale R, Dobbins B, Reed K, Dubos T. 2018. NCAR CESM2.0 release of CAM-SE: A reformulation of the spectral-element dynamical core in dry-mass vertical coordinates with comprehensive treatment of condensates and energy. *J. Adv. Model. Earth Syst.* doi:10.1029/2017MS001257.

Lauritzen PH, Taylor MA, Overfelt J, Ullrich PA, Nair RD, Goldhaber S, Kelly R. 2017. CAM-SE-CSLAM: Consistent coupling of a conservative semi-lagrangian finite-volume method with spectral element dynamics. *Mon. Wea. Rev.* **145**(3): 833–855, doi:10.1175/MWR-D-16-0258.1.

Lauritzen PH, Williamson DL. 2019. A total energy error analysis of dynamical cores and physics-dynamics coupling in the community atmosphere model (cam). *J. Adv. Model. Earth Syst.* doi:10.1029/2018MS001549.

Lindborg E. 1999. Can the atmospheric kinetic energy spectrum be explained by two-dimensional turbulence? *Journal of Fluid Mechanics* **388**: 259–288, doi:10.1017/s0022112099004851.

Liu X, Easter RC, Ghan SJ, Zaveri R, Rasch P, Shi X, Lamarque JF, Gettelman A, Morrison H, Vitt F, *et al.* 2012. Toward a minimal representation of aerosols in climate models: Description and evaluation in the community atmosphere model cam5. *Geoscientific Model Development* **5**(3): 709.

Medeiros B, Williamson DL, Olson JG. 2016. Reference aquaplanet climate in the community atmosphere model, version 5. *J. Adv. Model. Earth Syst.* **8**(1): 406–424, doi:10.1002/2015MS000593.

Nastrom GD, Gage KS. 1985. A climatology of atmospheric wavenumber spectra of wind and temperature observed by commercial aircraft. *J. Atmos. Sci.* **42**: 950–960.

Neale RB, Chen CC, Gettelman A, Lauritzen PH, Park S, Williamson DL, Conley AJ, Garcia R, Kinnison D, Lamarque JF, Marsh D, Mills M, Smith AK, Tilmes S, Vitt F, Cameron-Smith P, Collins WD, Iacono MJ, Easter RC, Ghan SJ, Liu X, Rasch PJ, Taylor MA. 2012. Description of the NCAR Community Atmosphere Model (CAM 5.0). NCAR Technical Note NCAR/TN-486+STR, National Center of Atmospheric Research.

Neale RB, Chen CC, Gettelman A, Lauritzen PH, Park S, Williamson DL, Conley AJ, Garcia R, Kinnison D, Lamarque JF, Marsh D, Mills M, Smith AK, Tilmes S, Vitt F, Cameron-Smith P, Collins WD, Iacono MJ, Easter RC, Ghan SJ, Liu X, Rasch PJ, Taylor MA. 2010. Description of the NCAR Community Atmosphere Model (CAM 4.0). NCAR Technical Note, National Center of Atmospheric Research.

Neale RB, Hoskins BJ. 2000. A standard test for agcms including their physical parametrizations: I: the proposal. *Atmos. Sci. Lett* **1**(2): 101–107, doi:10.1006/asle.2000.0022.

Neale RB, Richter JH, Jochum M. 2008. The impact of convection on ENSO: From a delayed oscillator to a series of events. *J. Climate* **21**: 5904–5924.

O'Brien TA, Collins WD, Kashinath K, Rübel O, Byna S, Gu J, Krishnan H, Ullrich PA. 2016. Resolution dependence of precipitation statistical fidelity in hindcast simulations. *J. Adv. Model. Earth Syst.* **8**(2): 976–990, doi:10.1002/2016ms000671, URL http://dx.doi.org/10.1002/2016ms000671.

Orlanski I. 1981. The quasi-hydrostatic approximation. *J. Atmos. Sci.* **38**: 572–582, doi:10.1175/1520-0469(1981)038⟨0572:TQHA⟩2.0.CO;2, URL http://dx.doi.org/10.1175/1520-0469(1981)038<0572:TQHA>2.0.CO;2.

Pauluis O, Garner S. 2006. Sensitivity of radiative–convective equilibrium simulations to horizontal resolution. *J. Atmos. Sci.* **63**(7): 1910–1923.

Plant RS, Craig GC. 2008. A stochastic parameterization for deep convection based on equilibrium statistics. *J. Atmos. Sci.* **65**: 87–105, doi:10.1175/2007JAS2263.1, URL http://dx.doi.org/10.1175/2007JAS2263.1.

Pope V, Stratton R. 2002. The processes governing horizontal resolution sensitivity in a climate model. *Climate Dynamics* **19**(3-4): 211–236.

Rauscher SA, O'Brien TA, Piani C, Coppola E, Giorgi F, Collins WD, Lawston PM. 2016. A multimodel intercomparison of resolution effects on precipitation: simulations and theory. *Climate Dynamics* **47**(7-8): 2205–2218, doi:10.1007/s00382-015-2959-5.

Rauscher SA, Ringler TD, Skamarock WC, Mirin AA. 2013. Exploring a global multiresolution modeling approach using aquaplanet simulations. *Journal of Climate* **26**(8): 2432–2452, doi:10.1175/jcli-d-12-00154.1.

Raymond DJ, Blyth AM. 1992. Extension of the stochastic mixing model to cumulonimbus clouds. *Journal of the Atmospheric Sciences* **49**(21): 1968–1983, doi:10.1175/1520-0469(1992)049⟨1968:eotsmm⟩2.0.co;2.

Richter JH, Rasch PJ. 2008. Effects of convective momentum transport on the atmospheric circulation in the community atmosphere model, version 3. *J. Climate* **21**(7): 1487–1499.

Satoh M, Matsuno T, Tomita H, Miura H, Nasuno T, Iga S. 2008. Nonhydrostatic icosahedral atmospheric model (NICAM) for global cloud resolving simulations. *J. Comput. Phys.* : 3486–3514.

Skamarock W. 2011. Kinetic energy spectra and model filters, in: P.H. Lauritzen, R.D. Nair, C. Jablonowski, M. Taylor (Eds.), Numerical techniques for global atmospheric models. *Lecture Notes in Computational Science and Engineering, Springer* **80**.

Skamarock WC, Klemp JB, Duda MG, Fowler L, Park SH, Ringler TD. 2012. A multi-scale nonhydrostatic atmospheric model using centroidal Voronoi tesselations and C-grid staggering. *Mon. Wea. Rev.* **240**: 3090–3105, doi: doi:10.1175/MWR-D-11-00215.1.

Skamarock WC, Park SH, Klemp JB, Snyder C. 2014. Atmospheric kinetic energy spectra from global high-resolution nonhydrostatic simulations. *Journal of the Atmospheric Sciences* **71**(11): 4369–4381, doi:10.1175/JAS-D-14-0114.1.

Song F, Zhang GJ. 2018. Understanding and improving the scale dependence of trigger functions for convective parameterization using cloud-resolving model data. *Journal of Climate* **31**(18): 7385–7399.

Takahashi YO, Hamilton K, Ohfuchi W. 2006. Explicit global simulation of the mesoscale spectrum of atmospheric motions. *Geophys. Res. Lett.* **33**(12), doi:10.1029/2006gl026429, URL http://dx.doi.org/10.1029/2006gl026429.

Taylor MA, Fournier A. 2010. A compatible and conservative spectral element method on unstructured grids. *J. Comput. Phys.* **229**(17): 5879 – 5895, doi: 10.1016/j.jcp.2010.04.008.

Terai C, Caldwell P, Klein S. 2016. Why do climate models drizzle too much and what impact does this have? In: *AGU Fall Meeting Abstracts*.

Terai CR, Caldwell PM, Klein SA, Tang Q, Branstetter ML. 2018. The atmospheric hydrologic cycle in the acme v0. 3 model. *Climate dynamics* **50**(9-10): 3251–3279.

Ullrich PA, Jablonowski C, Kent J, Lauritzen PH, Nair R, Reed KA, Zarzycki CM, Hall DM, Dazlich D, Heikes R, Konor C, Randall D, Dubos T, Meurdesoif Y, Chen X, Harris L, Kühnlein C, Lee V, Qaddouri A, Girard C, Giorgetta M, Reinert D, Klemp J, Park SH, Skamarock W, Miura H, Ohno T, Yoshida R, Walko R, Reinecke A, Viner K. 2017. ”dcmip2016: A review of non-hydrostatic dynamical core design and intercomparison of participating models”. *Geosci. Model Dev.* **10**: 4477–4509, doi:10.5194/gmd-10-4477-2017.

Weisman ML, Skamarock WC, Klemp JB. 1997. The resolution dependence of explicitly modeled convective systems. *Monthly Weather Review* **125**(4): 527–548, doi:10.1175/1520-0493(1997)125⟨0527:TRDOEM⟩2.0.CO;2.

Wilks DS. 2011. *Statistical methods in the atmospheric sciences*, vol. 100. Academic press.

Williamson DL. 2008. Convergence of aqua-planet simulations with increasing resolution in the community atmospheric model, version 3. *Tellus A* **60**(5): 848–862, doi:10.1111/j.1600-0870.2008.00339.x.

Williamson DL. 2013. The effect of time steps and time-scales on parametrization suites. *Quart. J. Roy. Meteor. Soc.* **139**(671): 548–560, doi: 10.1002/qj.1992.

Williamson DL, Kiehl JT, Hack JJ. 1995. Climate sensitivity of the ncar community climate model (ccm2) to horizontal resolution. *Climate Dynamics* **11**(7): 377–397, doi:10.1007/s003820050082.

Xie S, Wang YC, Lin W, Ma HY, Tang Q, Tang S, Zheng X, Golaz JC, Zhang GJ, Zhang M. 2019. Improved diurnal cycle of precipitation in e3sm with a revised convective triggering function. *Journal of Advances in Modeling Earth Systems* .

Xie S, Zhang M. 2000. Impact of the convection triggering function on single-column model simulations. *Journal of Geophysical Research: Atmospheres* **105**(D11): 14 983–14 996.

Zarzycki CM, Levy MN, Jablonowski C, Overfelt JR, Taylor MA, Ullrich PA. 2014. Aquaplanet experiments using cam's variable-resolution dynamical core. *J. Climate* **27**(14): 5481–5503, doi:10.1175/JCLI-D-14-00004.1.

Zhang G, McFarlane N. 1995. Sensitivity of climate simulations to the parameterization of cumulus convection in the canadian climate centre general circulation model. *Atmosphere-ocean* **33**(3): 407–446.

Zhang GJ. 2002. Convective quasi-equilibrium in midlatitude continental environment and its effect on convective parameterization. *Journal of Geophysical Research: Atmospheres* **107**(D14): ACL–12.

Zängl G, Reinert D, Rípodas P, Baldauf M. 2014. The icon (icosahedral non-hydrostatic) modelling framework of dwd and mpi-m: Description of the non-hydrostatic dynamical core. *Quarterly Journal of the Royal Meteorological Society* **141**(687): 563–579, doi:10.1002/qj.2378.

